Nonuniform Distribution of Crystalline Phases and Grain Sizes in the Surface Layers of WC Ceramics Produced by Spark Plasma Sintering

Ksenia E. Smetanina *, Pavel V. Andreev *, Evgeny A. Lantsev, Aleksey V. Nokhrin, Artem A. Murashov, Natalia V. Isaeva, Yury V. Blagoveshchensky, Maksim S. Boldin, Vladimir N. Chuvil'deev

Posted Date: 16 May 2023

doi: 10.20944/preprints202305.1121.v1

Keywords: tungsten carbide; spark plasma sintering; diffusion; carbon

Article

Nonuniform Distribution of Crystalline Phases and Grain Sizes in the Surface Layers of WC Ceramics Produced by Spark Plasma Sintering

Ksenia E. Smetanina [1,*], Pavel V. Andreev [1,*], Evgeny A. Lantsev [1], Aleksey V. Nokhrin [1], Artem A. Murashov [1], Natalia V. Isaeva [1,2], Yury V. Blagoveshchensky [2], Maksim S. Boldin [1] and Vladimir N. Chuvil'deev [1]

[1] Materials Science Department, Research Institute of Physics and Technology, Lobachevsky State University of Nizhny Novgorod, 603022 Nizhny Novgorod, Russia
[2] Laboratory of Plasma Processes in Metallurgy and Metal Processing, A.A. Baykov Institute of Metallurgy and Materials Science, Russian Academy of Sciences, 119334 Moscow, Russia
* Correspondence: andreev@phys.unn.ru (P.V.A.) smetanina@nifti.unn.ru (K.E.S.)

Abstract: The research results conducted on binderless tungsten carbide (WC) ceramics obtained by Spark Plasma Sintering (SPS) of WC powders with different average particle sizes (0.095, 0.8, 3 μm) are presented. Nonuniform distribution of crystalline phases and microstructure of the WC ceramics was studied using layer-by-layer XRD analysis and SEM. Surface layers of the WC-based ceramics are characterized by nonuniform distribution of W_2C crystalline phase and grain sizes, including the appearance of abnormally large grains. Thickness of the nonuniform layer was at least 50 μm. The effect under study is associated with an intense carbon diffusion from graphite foil. On the one hand, this contributed to a decrease in the intensity of W_2C phase particle formation, which is transformed into α-WC phase due to the carbon. On the other hand, it caused abnormal grain growth in the layer where the carbon diffused. The obtained value of the carbon diffusion depth exceeds the values known from the literature (up to 1 μm in the case of volume diffusion even at temperature of 2370℃ and exposure time of ~ 60 h). The use of boron nitride (BN) as a protective coating on graphite mold parts did not prevent the formation of nonuniform layer on the ceramic surface.

Keywords: tungsten carbide; spark plasma sintering; diffusion; carbon

1. Introduction

Hard alloys based on tungsten carbide (WC) with the addition of cobalt (Co), iron (Fe), nickel (Ni) and other low-melting metal phases are used in mechanical engineering for the production of wire drawing dies, drill bits and other wear-resistant machine elements [1–4]. Tungsten carbide is characterized by high hardness, wear resistance, melting point as well as chemical resistance to acids and alkalis [1, 5]. The combination of these properties allows the use of WC-based ceramics at high temperatures and under heavy loads. However, binderless tungsten carbide has a low fracture toughness and bending strength [5]. New technologies for producing high-strength binderless WC ceramics attract researchers' attention for this reason [5–8].

Spark Plasma Sintering (SPS) is one of the most promising methods of manufacturing high-density fine-grained ceramics and hard alloys [3–5,9,10]. The technology consists of high-speed heating of conductive mold filled with initial powder or green body by passing millisecond current pulses (up to 5000 A) with simultaneous application of uniaxial load [9,11–13]. High speed of heating (up 2500 ℃/min) is provided by the use of pulse mode. This approach makes it possible to reduce the sintering time and keep the grain size in ceramics close to the particle size of initial powder. The advantage of SPS is the ability to control and manage key technological parameters directly during the sintering process – the applied stress, the heating rate, the sintering temperature, the time of isothermal exposure, the cooling rate. This ensures effective control of microstructure parameters and performance properties of ceramics and hard alloys. Descriptions of the SPS features has been

 doi:10.20944/preprints202305.1121.v1

considered in detail in previous studies [11–13]. The effectiveness of SPS technology use for sintering ceramics and hard alloys based on tungsten carbide has been demonstrated in several studies [3–5,10].

The use of WC nanopowders for the production of ceramics and hard alloys provides additional opportunities to optimize their phase composition, microstructure parameters and improve mechanical properties. One of the most promising methods for producing WC nanopowders is the DC arc plasma chemical synthesis [14]. The method allows to obtain tungsten monocarbide (α-WC) powders with an average particle size of 30-80 nm. Previous studies have reported that binderless ceramics obtained by SPS of plasma chemical nanopowders WC are characterized by high hardness (up to 30 GPa) and fracture toughness (4-5 MPa·m$^{1/2}$) [5]. WC – Co hard alloys made by sintering of plasma chemical nanopowders WC also had high hardness [15].

Recent studies suggest that ceramics and hard alloys produced by SPS of WC nanopowders have nonuniform microstructure [15–17]. The method of layer-by-layer X-ray diffraction analysis (XRD) is the most effective way to study this issue [16,17]. The XRD information depth is about 5 μm at the CuKα wavelength (λ = 1.54 Å) due to the high absorption of X-ray radiation in phases containing tungsten. Sequential removal of layers will allow to carry out phase analysis of ceramics at different distances from the surface. The distribution of η-phase (Co_3W_3C) over the depth of WC + 10% wt. Co hard alloys was investigated using the technique of layer-by-layer XRD. It was found that there is no η-phase (Co_3W_3C) in the surface layer about 300-350 μm in thickness [17]. Similar results were obtained for binderless WC ceramics [16]. It is assumed that the surface layer heterogeneity of ceramics and hard alloys based on WC is due to the intense carbon diffusion from graphite foil and graphite mold used in SPS [16,17]. The carbon contamination effect of the surface layers of ceramics during SPS has also been described in several studies [12,18–20].

The carbon contamination is considered as a negative effect that affects many characteristics of different ceramics [12,19–23]. As a result of this effect, the optical properties of oxide ceramics can be reduced [20–23]. At the same time, carburization of the surface layers in ceramics and hard alloys based on WC can lead to a decrease in the content of undesirable phases and, as a result, contribute to an increase in hardness [17,24].

W–C system is characterized by the presence of a very narrow range of temperatures and concentrations corresponding to the area of stable existence of α-WC phase [25]. Even a slight deviation of the carbon content from the stoichiometric composition (6.13% wt.) leads to the appearance of undesirable W_2C phase in WC ceramics or to the formation of η-phases (Co_2W_4C, Co_3W_3C, Co_6W_6C, $Co_3W_9C_4$) in WC–Co hard alloys [5,15,17,25].

Adsorbed oxygen is present on the surface of WC powder particles [26]. Tungsten carbide nanopowders are characterized by increased oxygen concentration [26,27]. Oxygen reacts with carbon in carbide particles to form carbon dioxide, W_2C phase and/or tungsten oxide in the process of heating WC powder [27]. The problem of decarbonization is partially solved by introducing a small amount of graphite into the raw WC powder [15,17,27]. This decision avoids the formation of undesirable phases and leads to an increase in the mechanical properties of ceramics and hard alloys. However, excessive graphite content in the raw WC powder can lead to rapid grain growth and negatively affects the mechanical properties of WC-based materials [5,15,17,28,29]. The exact determination of the required graphite content is a difficult task. The oxygen concentration may increase during long-term storage of the powder or working with it in an environment containing oxygen.

The purpose of the work is a detailed study of the heterogeneity of the surface layers of the binderless tungsten carbide ceramics produced by SPS.

2. Materials and Methods

Three tungsten carbide (WC) powders with different average particle sizes were used as raw materials. Nanopowder #1 was prepared by DC arc plasma chemical synthesis [14]. Powders #2 and #3 are industrial micron powders produced by Kirovgrad Plant of Hard Alloys, JSC (Kirovgrad,

Preprints (www.preprints.org) | NOT PEER-REVIEWED | Posted: 16 May 2023 doi:10.20944/preprints202305.1121.v1

Russia). Carbon and oxygen content in the raw powders was determined using an analyzer CS 400 (LECO, Michigan, USA). The characteristics of the WC powders are presented in Table 1.

Table 1. The characteristics of the WC powders.

Powder	1	2	3
Average particle size, μm	0.095	0.8	3
Oxygen content, % wt.	0.40 ± 0.01	0.25 ± 0.01	0.12 ± 0.01
Carbon content, % wt.	6.32 ± 0.01	6.14 ± 0.01	6.13 ± 0.01
Content of α-WC, % wt.	97.4 ± 0.2	98.6 ± 0.2	98.4 ± 0.2
Content of W_2C, % wt.	–	1.4 ± 0.2	1.6 ± 0.2
Content of W, % wt.	2.6 ± 0.2	–	–

The concentration of oxygen in Nanopowder #1 was elevated. Carbon was added in the form of graphite (0.3% wt.) by the manufacturer to the composition of powder #1 to eliminate the negative effects of oxygen. Powders #2 and #3 also contained 0.05% wt. of graphite.

The powders were poured into a graphite mold with an inner diameter of 12.8 mm, an outer diameter of 30 mm and a height of 30 mm. The uniaxial stress was applied to the mold using two graphite punches. The punch diameter was 12 mm, height was 20 mm. Graphite foil with a thickness of 200 μm was used to reduce the clearance between the specimen and the inner surface of the mold. Two sheets of graphite foil were placed between the powder and the punch surface. Preliminary pressing of the powders in mold was carried out using a hydraulic press Sorokin (Sorokin, Moscow, Russia) at room temperature at a stress of 70 MPa.

SPS of the WC powders was conducted using Dr. Sinter model SPS-625 setup (SPS Syntex, Tokyo, Japan). Figure 1 shows schematic setup of SPS system.

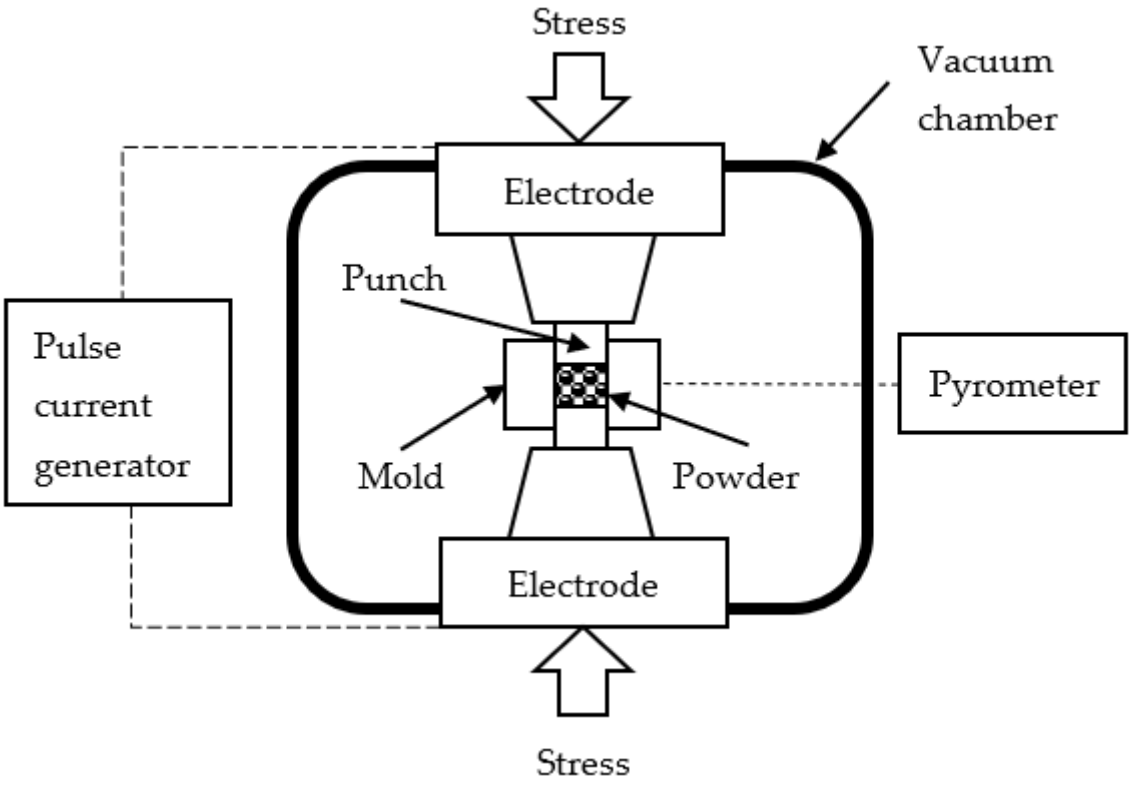

Figure 1. Basic SPS system configuration. Scheme.

Graphite mold were covered with graphite felt of 4 mm in thickness to ensure the homogeneity of the temperature field during sintering inside the mold. A hole with a diameter of 14 mm was cut into the graphite felt for the temperature control during SPS. The temperature was measured using

Preprints (www.preprints.org) | NOT PEER-REVIEWED | Posted: 16 May 2023 doi:10.20944/preprints202305.1121.v1

an optical pyrometer IR-AHS2 (Chino, Tokyo, Japan) focused on the height middle of the mold outer wall. The accuracy of temperature measurements was ± 20°C. SPS of the WC powders was carried out in a vacuum (about 6 Pa) under a uniaxial compressive stress of 70 MPa. The powders were heated at the rate of 50°C/min until the end temperature of the effective shrinkage of the powders: 1410°C (powder #1), 1530°C (powder #2), 1625°C (powder #3). There was no exposure at the sintering temperature. Free cooling was used to cool the specimens.

The comparison objects were WC ceramics produced by sintering in graphite molds with a protective coating of boron nitride (BN). Solution of BN was applied to the inner surfaces of the graphite parts (mold, punches, foil) that contact with the powder during SPS.

The dependencies of the effective powder shrinkage (L_{eff}) on the heating temperature were recorded during sintering using a built-in dilatometer of Dr. Sinter model SPS-625. Experiments on heating an empty mold were carried out to account for the contribution of thermal expansion of the graphite mold (L_0). The true shrinkage (L) was determined by the formula: $L = L_{eff} - L_0$.

The initial heights of the ceramics did not exceed 6 mm. The specimen surface was sequentially ground with diamond discs and polished with diamond pastes. Grinding was carried out on the Secotom 10 machine (Struers, Copenhagen, Denmark). Polishing was performed on the AutoMet 250 machine (Buehler, Braunschweig, Germany). Eleven stages of the mechanical treatment of the specimen surface were carried out. Each stage consisted of grinding and polishing. The layer up to 50 μm in thickness (stages #1-7) and the layer at least 200 μm in thickness (stages #8-11) was removed from the specimen surface in each treatment stage. In total, the layer about 1100-1200 μm in thickness was removed from the surface of each specimen. The height control of the specimens was carried out using a micrometer 34480-25_z01 (ZUBR, Moscow, Russia) with an accuracy equal to 10 μm.

XRD studies of the powders and ceramics were carried out on the XRD-7000 diffractometer (Shimadzu, Kyoto, Japan) in CuKα radiation (λ = 1.54 Å). Scanning was performed in the Bragg-Brentano geometry in the range of angles 2θ = 30–80° with the step of 0.04° and the exposure of 2 s. XRD experiments were carried out after each stage of the specimen surface treatment (stages #1-11). The XRD experiment of stage #0 was conducted before the mechanical treatment of the specimen surface. The calculated penetration depth of CuKα radiation into the surface of WC specimens does not exceed 5 μm, which is much less than the thickness of the removed layer during the mechanical grinding (50-200 μm). Qualitative phase analysis was carried out using the PDF-2 database (ICDD, 2012): α-WC (PDF 00-051-0939), W_2C (PDF 00-035-0776), W (PDF 00-004-0806), C (PDF 00-056-0159), WB (PDF 00-006-0541), BN (PDF 01-085-1068). Quantitative phase analysis was carried out by the reference ratio method using cif-files of the ICSD (2015): α-WC (ICSD 43380), W_2C (ICSD 159904), W (ICSD 76151). The diffraction peak (101) at 2θ = 48.3° was chosen as the analytical peak of α-WC phase during the quantitative analysis. The analytical peaks of W_2C and W phases were (101) at 2θ = 39.6° and (110) at 2θ = 40.3° respectively.

The microstructure of the powders and ceramics was studied by scanning electron microscopy (SEM) on a microscope Jeol JSM-6490 (Jeol, Tokyo, Japan). After the sixth stage of the mechanical treatment of the surface and removal of the layer of 150 μm in thickness, the control specimens were cut in half, as shown in Figure 2a. The cross section was polished with diamond pastes. Figure 2b shows the areas under study. In particular, D area was located on the surface that was subjected to the mechanical treatment.

Preprints (www.preprints.org) | NOT PEER-REVIEWED | Posted: 16 May 2023 doi:10.20944/preprints202305.1121.v1

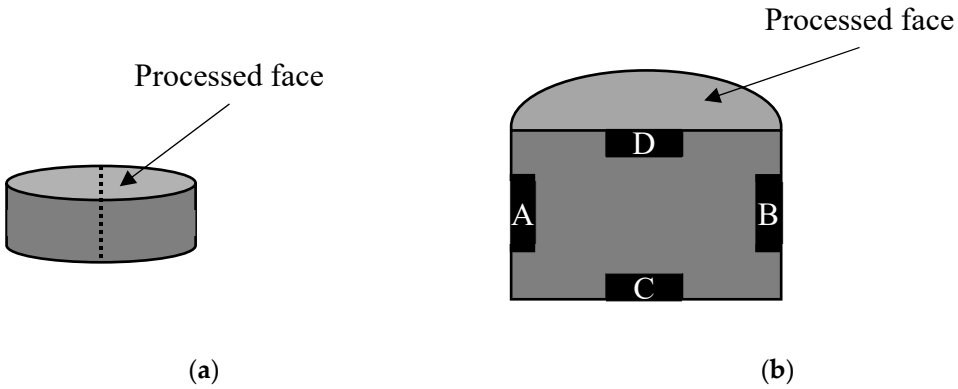

Figure 2. Cutting scheme **(a)** and location of cross section areas under study **(b)** of the WC ceramics.

In total, 9 ceramic specimens were sintered and studied. Powders #2 and #3 were sintered twice to control the reproducibility of the measurement results.

Specimens produced from powders #1, #2, #3 are referred to as ceramics #1, #2, #3. Specimen labeling Ceramic 2-1 means that the specimen #1 produced from powder #2 is described. Specimen labeling Ceramic 2-1-BN means that the specimen #1 produced from powder #2 using a protective coating of boron nitride is described. Such labeling of the specimens is used to demonstrate the reproducibility of the results. The result reproducibility was evaluated based on a comparison of the specimens sintered under the same conditions.

3. Results

3.1. Characterization of the WC powders

Figure 3 shows the results of the SEM studies of the WC initial powders. Agglomerates of individual nanoparticles are observed in powder #1 (Figure 3a). The size of the agglomerates does not exceed 10 μm. No agglomerates were found in powders #2 и #3 (Figure 3b, c). The average particle size of powders #2 and #3 is 1 μm and 3 μm respectively. The specified values of the average particle size determined by the chord method are close to the average particle size according to Fischer, declared by the powder manufacturer.

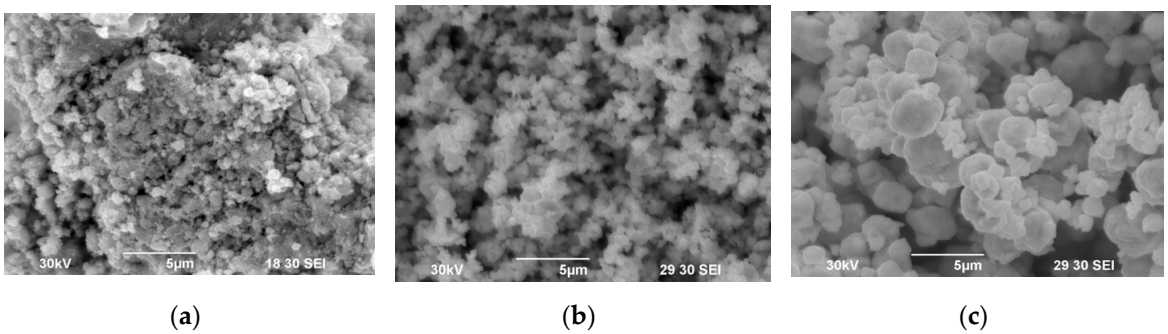

Figure 3. SEM images of WC powder #1 (**a**), #2 (**b**), #3 (**c**).

Figure 4 presents the results of the XRD studies of the WC powders. The diffraction peaks on the pattern of powder #1 correspond to α-WC and α-W phases. The XRD peaks on the diffraction pattern of powder #1 are significantly broadened compared to the XRD peaks on the patterns of powders #2 and #3. The mass fraction of tungsten in plasma chemical nanopowder #1 is 2.6 ± 0.2% wt. (Table 1). The XRD peaks on the patterns of powders #2 and #3 correspond to α-WC and W_2C phases. The mass fraction of W_2C in powders #2 and #3 are 1.4 ± 0.2 and 1.6 ± 0.2% wt. respectively (Table 1).

Preprints (www.preprints.org) | NOT PEER-REVIEWED | Posted: 16 May 2023 doi:10.20944/preprints202305.1121.v1

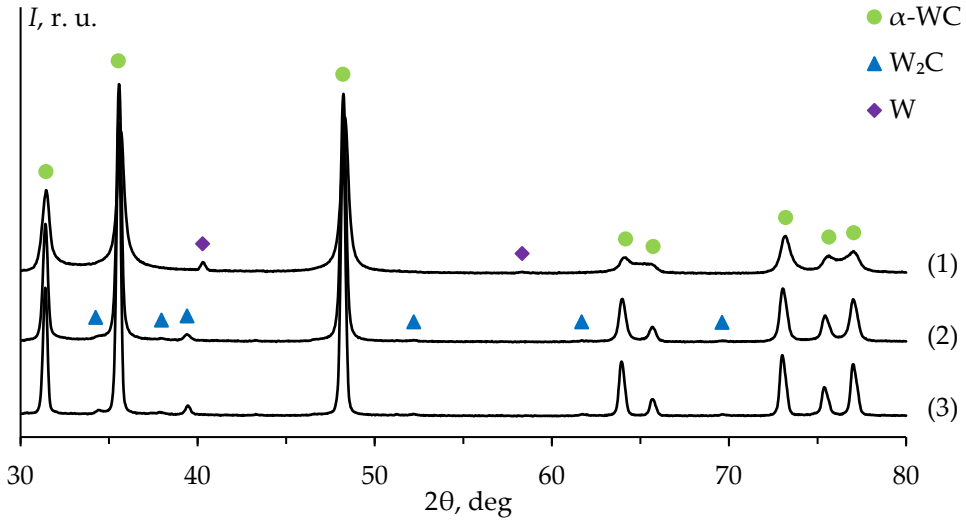

Figure 4. XRD patterns of WC powders #1-3. The pattern number corresponds to the powder number (Table 1).

3.2. SPS of the WC powders

Figure 5 shows graphical sintering diagrams of the ceramics sintered from powders #1-3 in the Process time (t) – Temperature (T) – Stress (P) coordinates. Stability and reproducibility of SPS process were ensured during the manufacture of specimens #2 and #3 (Figure 5b, c).

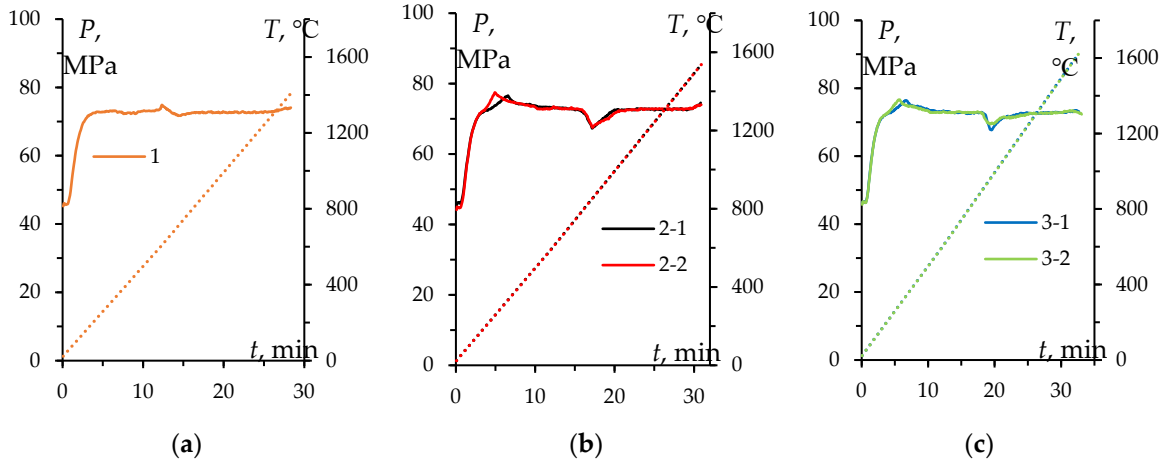

Figure 5. Sintering diagrams of ceramics #1 (**a**), #2 (**b**), #3 (**c**).

Figure 6 presents the temperature shrinkage curves $L(T)$ of the WC powders. The $L(T)$ curves have a conventional three-stage character for all powders: stage I – slight compaction at 600-1000°C, stage II – intensive shrinkage at 1000-1400°C, stage III – low shrinkage rate at above 1400°C. The difference in the absolute shrinkage (L_{max}) observed in Figure 6 is due to the difference in the bulk density of the powders under study. Previous investigation has reported a detailed analysis of SPS process of these powders [15].

Preprints (www.preprints.org) | NOT PEER-REVIEWED | Posted: 16 May 2023 doi:10.20944/preprints202305.1121.v1

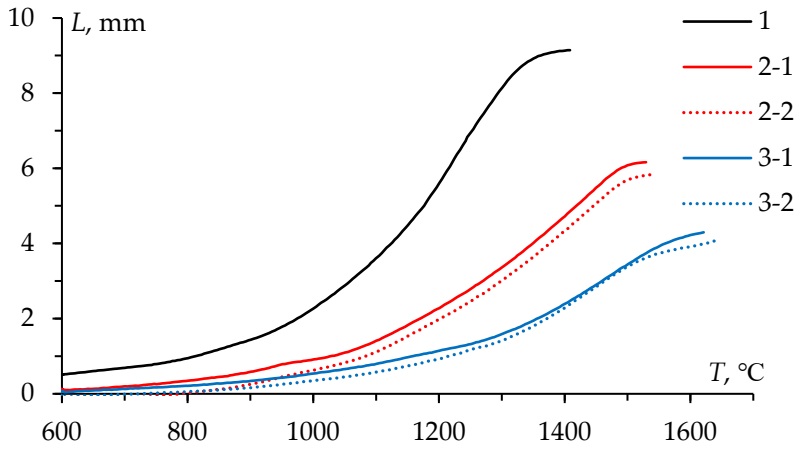

Figure 6. Temperature shrinkage curves $L(T)$ of WC powders 1-3.

The effective density of ceramics #1, #2, #3 was 99.2% (15.642 g/cm^3), 96.2% (15.168 g/cm^3), 96.0% (15.140 g/cm^3) respectively [15]. The specimens had no visible macrodefects such as chips, cracks or large pores. The specimens were not destroyed during the grinding and polishing process.

3.3. Layer-by-layer analysis of the WC ceramics

Figure 7 shows images of ceramic #1 after different stages of the surface mechanical treatment. The characteristic appearance of the ceramics with untreated initial surface (stage #0) is presented in Figure 7a. Graphite foil residues are visible on the specimen surface. This layer was removed during the initial mechanical treatment of the specimens (stage #1, Figure 7b). The gray metallic color characteristic of binderless tungsten carbide appeared after the second stage of the mechanical treatment (stage #2, Figure 7c).

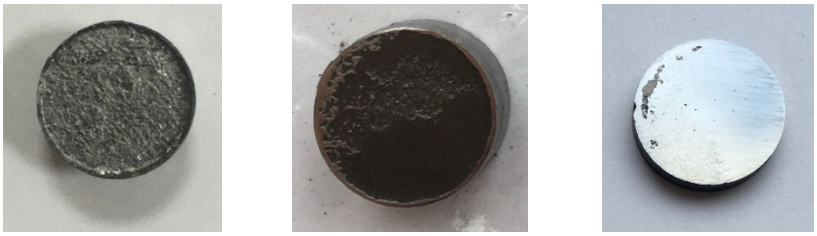

(**a**) (**b**) (**c**)

Figure 7. Appearance of ceramic #1 after various stages of the surface mechanical treatment: untreated initial surface – stage #0 (**a**), stage #1 (**b**), stage #2 (**c**).

Figure 8 shows the XRD patterns of ceramics #1-3 after each stage of the mechanical treatment, including the diffraction pattern of the untreated surface (stage #0, Figure 7a). The XRD peaks on the untreated surface pattern correspond to the α-WC and graphite phases. The high-intensity XRD peak of graphite on the diffraction pattern at $2\theta \approx 54°$ is explained by the presence of graphite foil residues on the untreated surface of the specimens (Figure 7a). The graphite peak on the diffraction pattern is not observed after the second stage of the surface mechanical treatment of ceramic #1 (Figure 8a) and after the third stage of the treatment of ceramics #2 and #3 (Figure 8b, c).

Preprints (www.preprints.org) | NOT PEER-REVIEWED | Posted: 16 May 2023 doi:10.20944/preprints202305.1121.v1

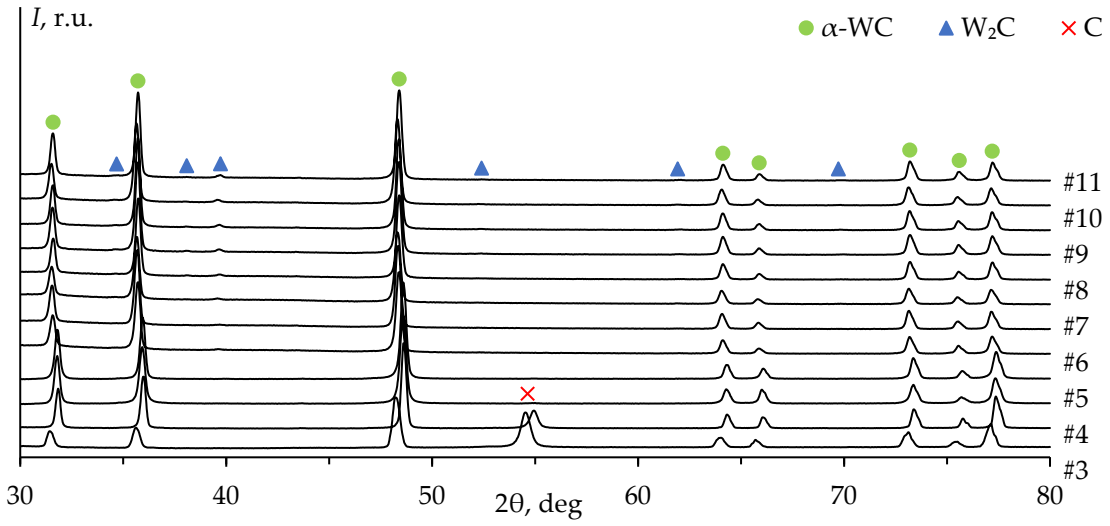

(**a**)

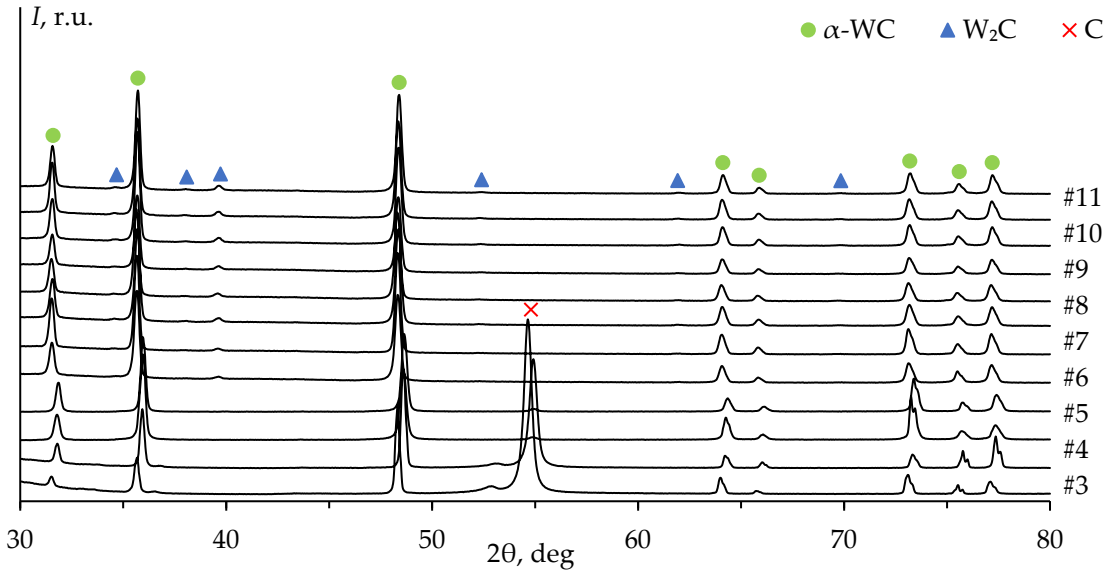

(**b**)

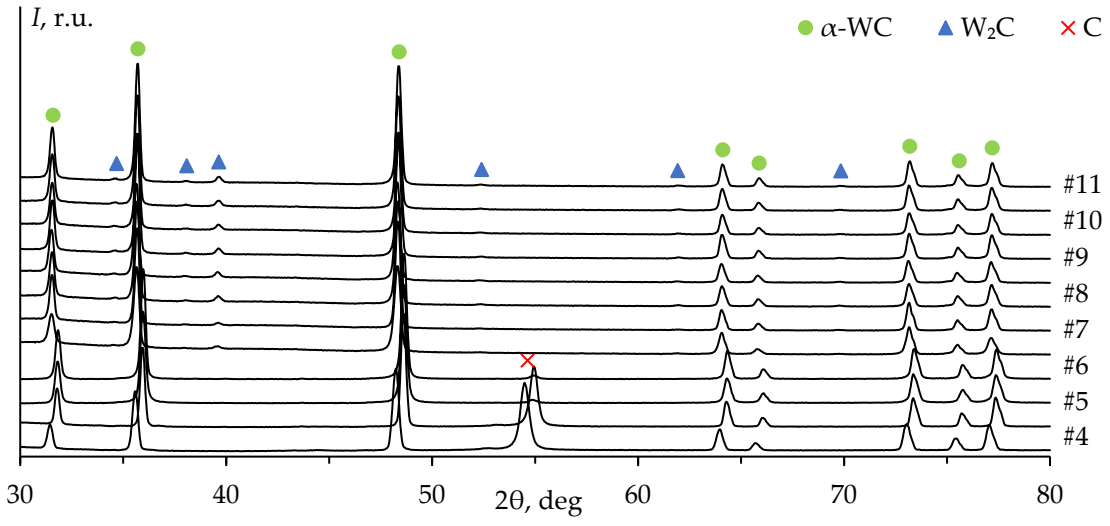

(**c**)

Figure 8. XRD patterns of ceramic 1 (**a**), 2 (**b**), 3 (**c**) after every stage of the surface treatment.

Preprints (www.preprints.org) | NOT PEER-REVIEWED | Posted: 16 May 2023 doi:10.20944/preprints202305.1121.v1

The diffraction peaks corresponding to W_2C phase are observed on the patterns starting from the fourth stage of the mechanical treatment. The intensity of W_2C peaks increases with the total removed layer thickness (Figure 9a). These results are similar to those of ceramics 2 and 3 (Figure 9b, c).

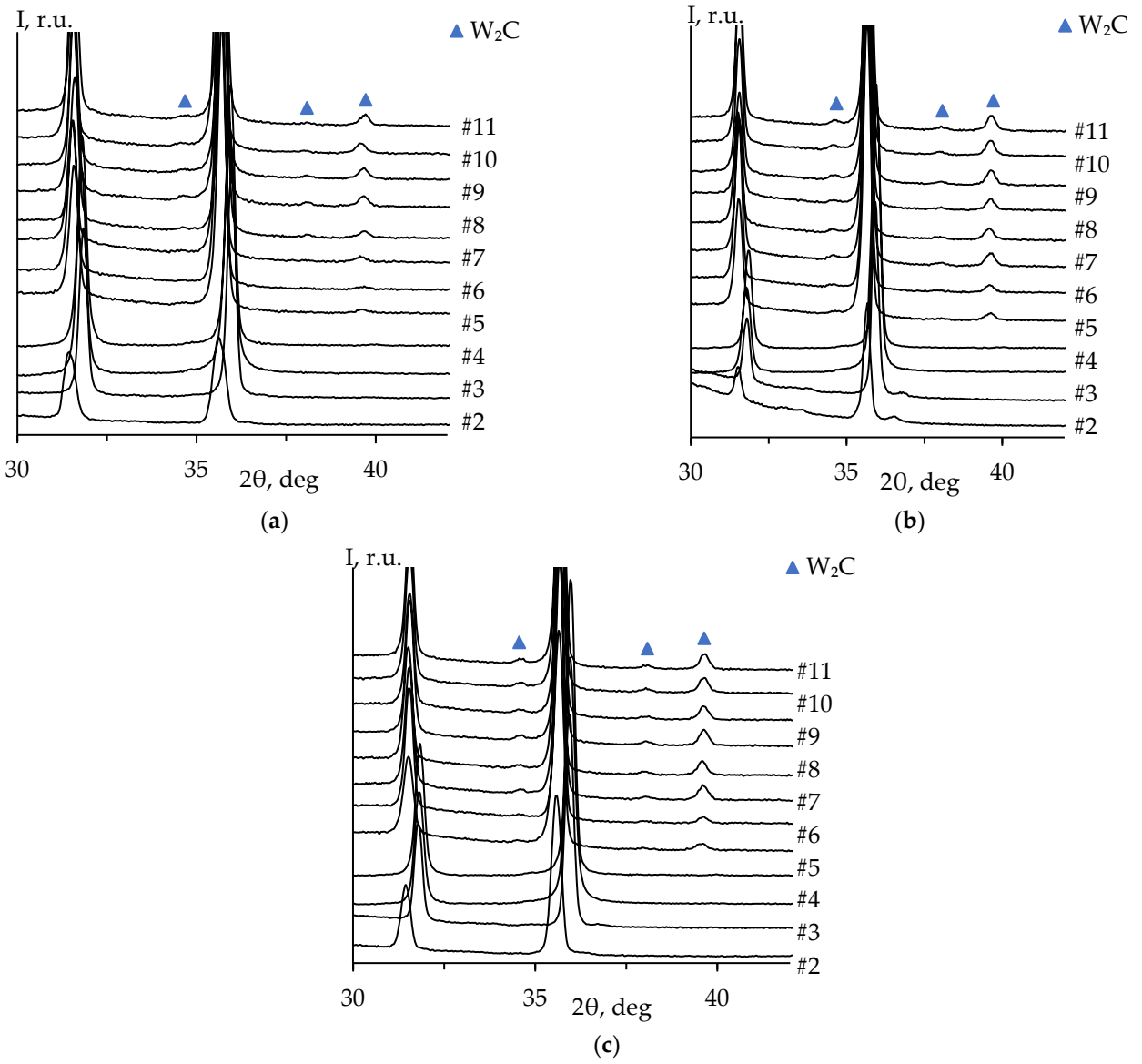

Figure 9. Sections of the XRD patterns of ceramic #1 (**a**), #2 (**b**), #3 (**c**) after various stages of the surface treatment.

Table 2 presents the results of the quantitative XRD of ceramics #1-3 after various stages of the surface mechanical treatment. It can be seen from the data in Table 2 that there is no difference (within the uncertainty) in the mass fraction of W_2C phase for the ceramics #2 and #3 sintered under the same conditions.

Table 2. Results of the quantitative XRD analysis of WC ceramics 1-3 depending on the stage of the surface treatment.

Stage	Content of W_2C, % wt.				
	Ceramic #1	Ceramics #2		Ceramics #3	
	Sample #1	Sample #2-1	Sample #2-2	Sample #3-1	Sample #3-2
#0 – 3	–	–	–	–	–

Preprints (www.preprints.org) | NOT PEER-REVIEWED | Posted: 16 May 2023 doi:10.20944/preprints202305.1121.v1

#4	0.9 ± 0.2	1.6 ± 0.2	1.0 ± 0.2	2.1 ± 0.2	1.4 ± 0.2
#5	0.7 ± 0.2	1.6 ± 0.2	1.2 ± 0.2	1.8 ± 0.2	1.7 ± 0.2
#6	1.3 ± 0.2	3.1 ± 0.2	3.5 ± 0.2	3.9 ± 0.2	4.1 ± 0.2
#7	1.5 ± 0.2	2.6 ± 0.2	(*)	3.9 ± 0.2	(*)
#8	2.1 ± 0.2	3.1 ± 0.2		3.7 ± 0.2	
#9	2.0 ± 0.2	3.1 ± 0.2		3.4 ± 0.2	
#10	2.0 ± 0.2	3.3 ± 0.2		4.0 ± 0.2	
#11	1.9 ± 0.2	3.1 ± 0.2		3.5 ± 0.2	

(*) The surface treatment of the specimen has been completed. The specimen was cut in accordance with the scheme shown in Figure 2b to the SEM study.

Figure 10-12 shows the results of the SEM studies of ceramics 1-3. Ceramics 2-2 and 3-2 were examined according to the scheme shown in Figure 2.

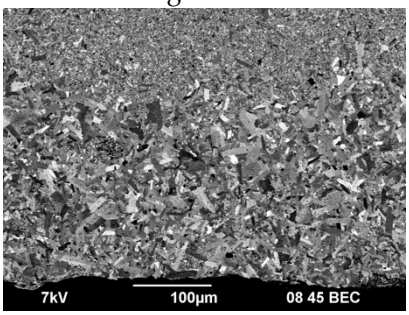

Figure 10. Microstructure of ceramic #1. SEM.

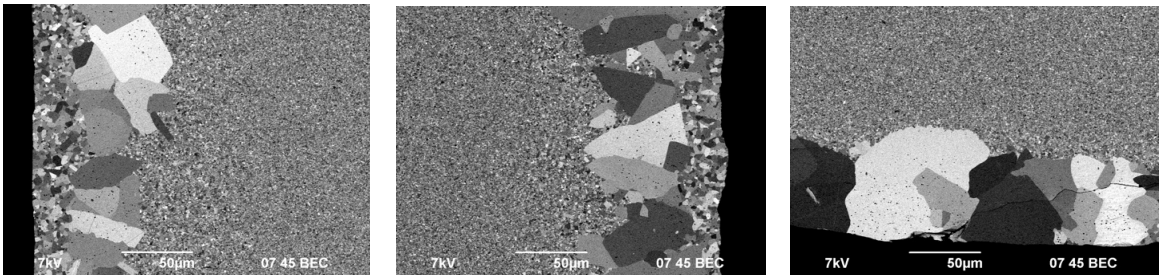

(**a**) (**b**) (**c**)

Figure 11. Microstructure of ceramic #2 cross section: area A (**a**), area B (**b**), area C (**c**). SEM.

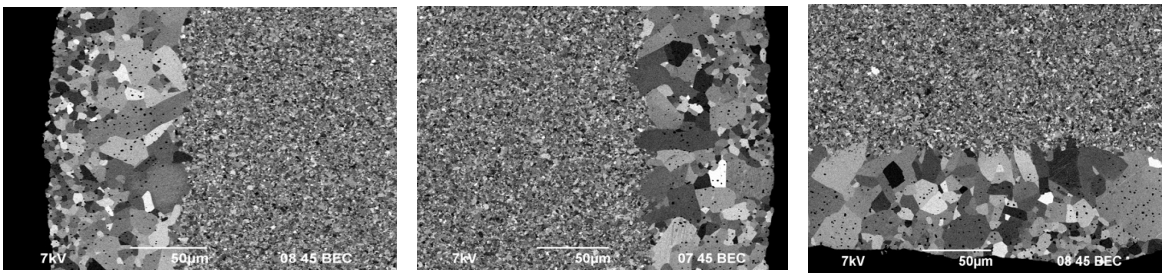

(**a**) (**b**) (**c**)

Figure 12. Microstructure of ceramic #3 cross section: area A (**a**), area B (**b**), area C (**c**). SEM.

As can be seen in Figure 10-12, the surface layers of the ceramics are characterized by nonuniform distribution of grain sizes, including the presence of abnormally large grains. Areas with non-uniform grain size distribution have a clear boundary. The thickness of the layers is 50-100 µm. The size of abnormally large grains reaches 50 µm. Abnormally large grains can be observed at the very edge of the specimen cross section (Figure 11c), which came in contact with a graphite foil during

Preprints (www.preprints.org) | NOT PEER-REVIEWED | Posted: 16 May 2023 doi:10.20944/preprints202305.1121.v1

SPS. Also, there is another thin layer with a clear boundary, containing grains whose size exceeded the average one in the main volume of the specimens by 2-3 times (most prominently in Fig. 11a, b). Despite the difference in the sintering temperatures, there is no difference in the surface layer depth in ceramics #2 and #3. The grains in the surface layer of ceramic #1 (Figure 10a) are mostly elongated. The average size of the abnormally large grains in ceramics 1 is much smaller than the one in ceramics 2 and 3.

A number of researchers have reported about abnormal grain growth in tungsten carbide at SPS [5,28,29]. Abnormal grain growth is also often detected in the study of WC–Co hard alloys [15,17,30–33]. Researchers note that increased concentration of carbon in powder is one of the key factors contributing to the appearance of large grains in fine-grained materials based on WC [30–33].

Thus, the analysis of the presented experimental results shows that the binderless tungsten carbide specimens obtained by SPS method have nonuniform microstructure and phase composition. It is presumed that the heterogeneity is due to the carburization of the surface layers of tungsten carbide.

3.4. Influence of BN coating on the phase composition and microstructure of the WC ceramics

To minimize the carburization effect of the surface layers, graphite molds with a protective coating of boron nitride on the inner surface were used. The protective coating was also applied to the graphite foil and to the punch surface. Figure 13 presents the temperature shrinkage curves $L(T)$ of the WC powders sintered in the graphite molds with BN coating. A comparison of the curves $L(T)$ shown in Figure 6 and Figure 13 reveals that there is no effect of BN coating on the character of the curves $L(T)$.

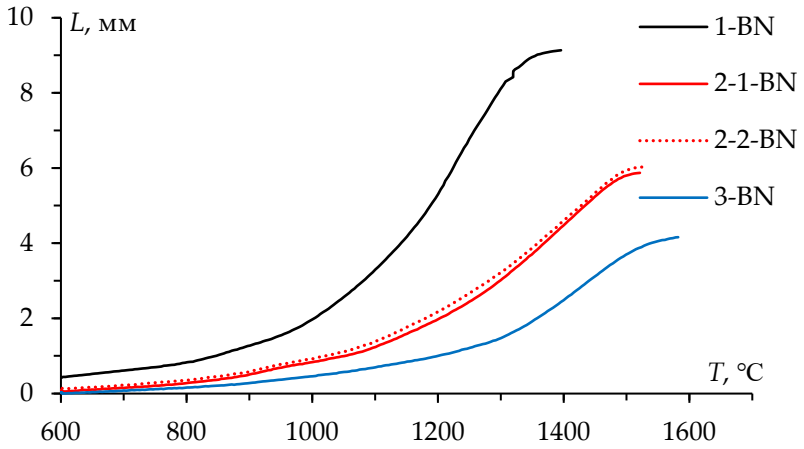

Figure 13. Temperature shrinkage curves L(T) of WC powders #1-3 sintered in the graphite molds coated with BN.

Figure 14 presents the XRD patterns of the untreated surface (stage #0) of ceramics #1-3 sintered in the graphite molds with BN coating. The XRD peaks of α-WC phase, graphite, tungsten boride WB (ICDD PDF 00-035-0738), boron nitride BN (ICDD PDF 01-085-1068) are observed on the diffraction patterns of the specimens.

Preprints (www.preprints.org) | NOT PEER-REVIEWED | Posted: 16 May 2023 doi:10.20944/preprints202305.1121.v1

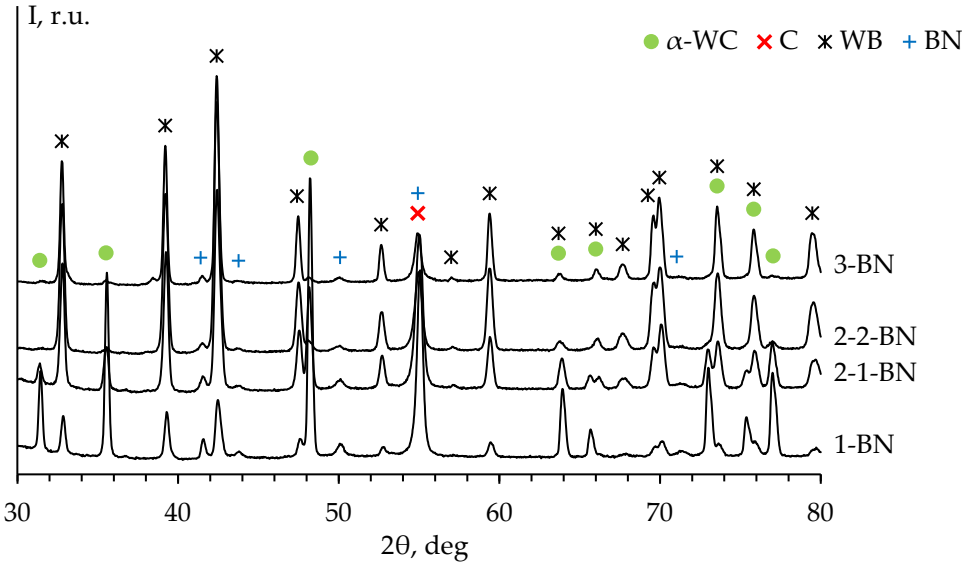

Figure 14. XRD patterns of the untreated initial surface (stage #0) of ceramics #1-3 sintered in the graphite molds coated with BN.

Traces of WB and BN phases are observed in all ceramics up to #3-4 stages of the surface mechanical treatment. At the same time, one of the most intense peaks of WB phase (at 2θ ≈ 39.2°) overlaps with the most intense peak of W_2C phase. In this regard, there is no reliable evidence that W_2C phase is present in the ceramics at stages #1-4 of the surface treatment. Full XRD patterns of the ceramics #1-3 sintered in the graphite molds with BN coating are presented in Figure 15.

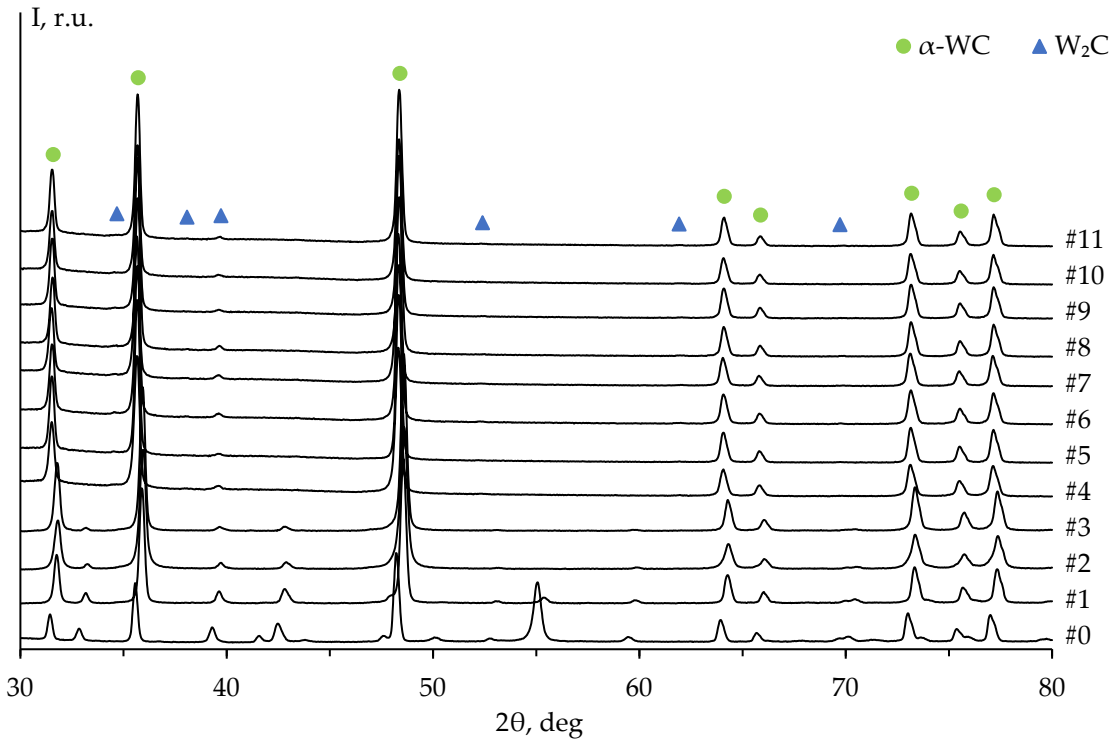

(**a**)

Preprints (www.preprints.org) | NOT PEER-REVIEWED | Posted: 16 May 2023 doi:10.20944/preprints202305.1121.v1

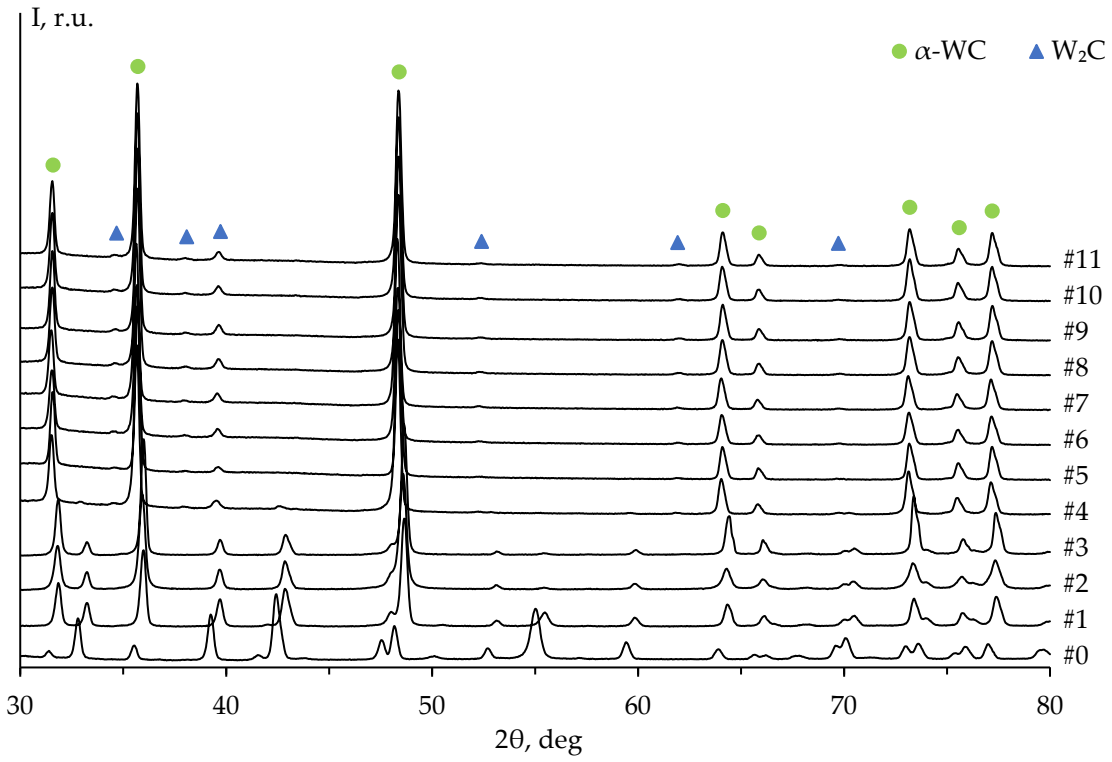

(**b**)

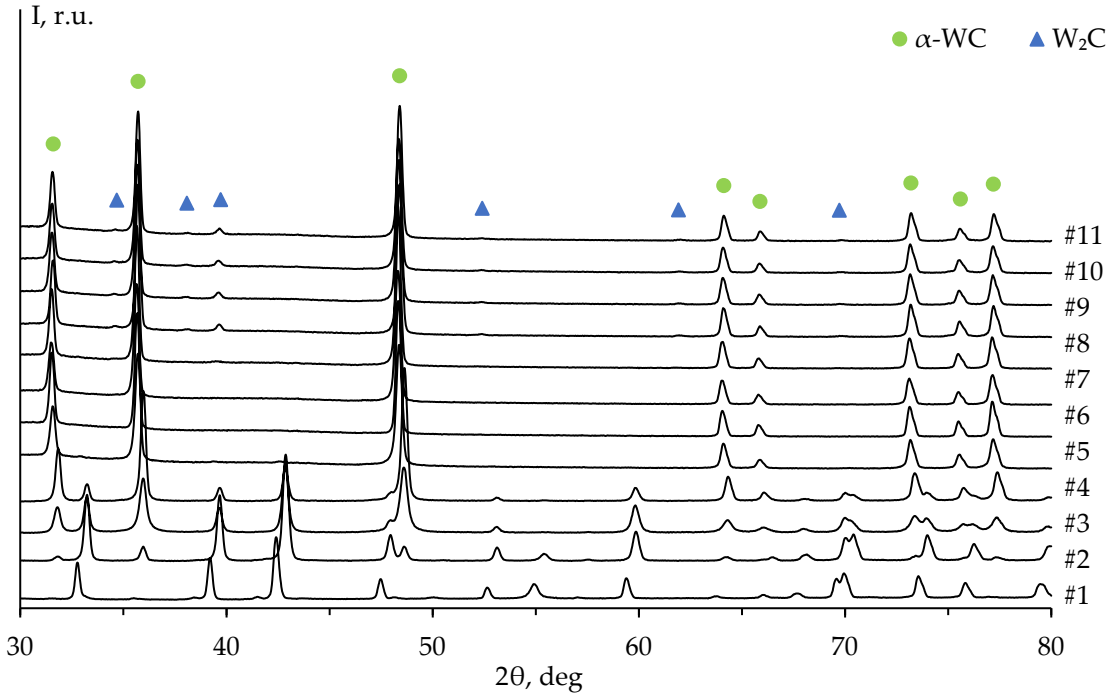

(**c**)

Figure 15. XRD patterns of ceramic #1 (**a**), #2 (**b**), #3 (**c**) sintered in the graphite molds coated with BN.

Figure 16 shows the results of the SEM investigation of microstructure at the edge of the lower face of ceramics #1-3 sintered in the graphite molds with BN coating.

Preprints (www.preprints.org) | NOT PEER-REVIEWED | Posted: 16 May 2023 doi:10.20944/preprints202305.1121.v1

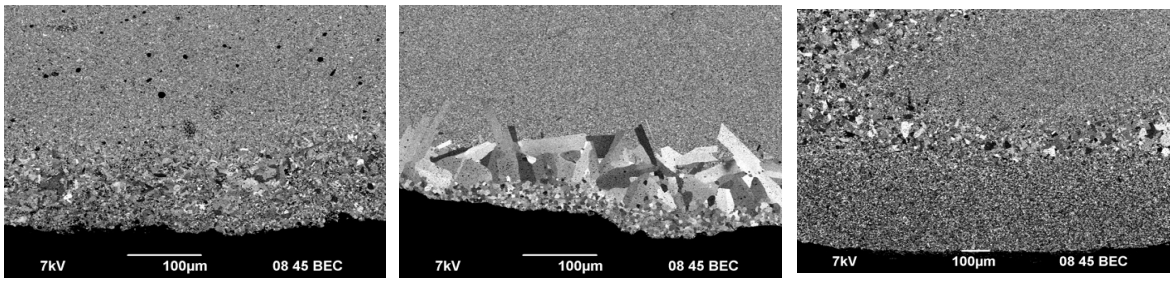

(**a**) (**b**) (**c**)

Figure 16. Microstructure of ceramic #1 (**a**), #2 (**b**), #3 (**c**).

Figure 17 presents the results of the SEM investigation (according to the scheme in Figure 2) of ceramics #2 cross section.

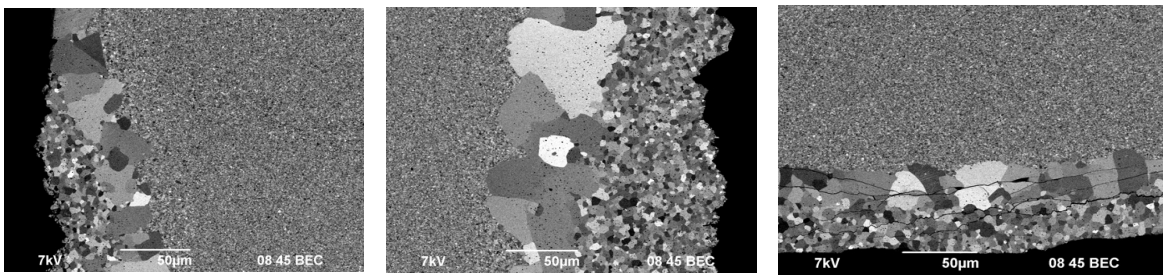

(**a**) (**b**) (**c**)

Figure 17. Microstructure of ceramic #2 cross section: area A (**a**), area B (**b**), area C (**c**). SEM.

Areas with non-uniform grain size distribution are observed on the ceramic surface sintered in the mold with BN coating (Figure 16, 17). The areas of non-uniform microstructure have a clear boundary between the layers. The area thickness varies from 50 to 150 µm (Figure 17a, b). Cracks observed in the surface layer indicates a low fracture toughness of this layer (Figure 17c).

4. Discussion

To analyze the results presented, it is necessary to consider the nature of the phase transformations in tungsten carbide-based ceramics at SPS previously. It is a widely held view that $W_2C \rightarrow \alpha$-WC phase change is possible only in the presence of excess carbon in accordance with the reaction [25,34]:

$$W_2C + C \rightarrow 2\ \alpha\text{-WC}. \quad (1)$$

As mentioned in the introduction to the paper, adsorbed oxygen is present on the surface of WC powder particles [26]. Oxygen reacts with carbon in WC carbide particles to form carbon dioxide (CO_2) in the process of heating WC powder:

$$2\ \alpha\text{-WC} + O_2 \rightarrow W_2C + CO_2\ (g). \quad (2)$$

This leads to a decrease in the carbon concentration in the carbide particles and the formation of W_2C phase particles. This process also known as decarbonization [27,35].

As was pointed out in the introduction, the existence of α-WC phase is a narrow carbon concentration range. The equilibrium carbon content in α-WC is 6.13% wt. Even a slight deviation of the carbon concentration from its equilibrium value leads to the formation of W_2C particles [25,27,35].

Figure 18 shows the distribution of the mass fraction of W_2C phase over the specimen depth in ceramics #1-3. It was taken into account that at the first stages of the treatment, the graphite foil residues were found on the specimen surface. In this regard, the depth reference point correction by the thickness of the layer containing graphite was made.

Preprints (www.preprints.org) | NOT PEER-REVIEWED | Posted: 16 May 2023 doi:10.20944/preprints202305.1121.v1

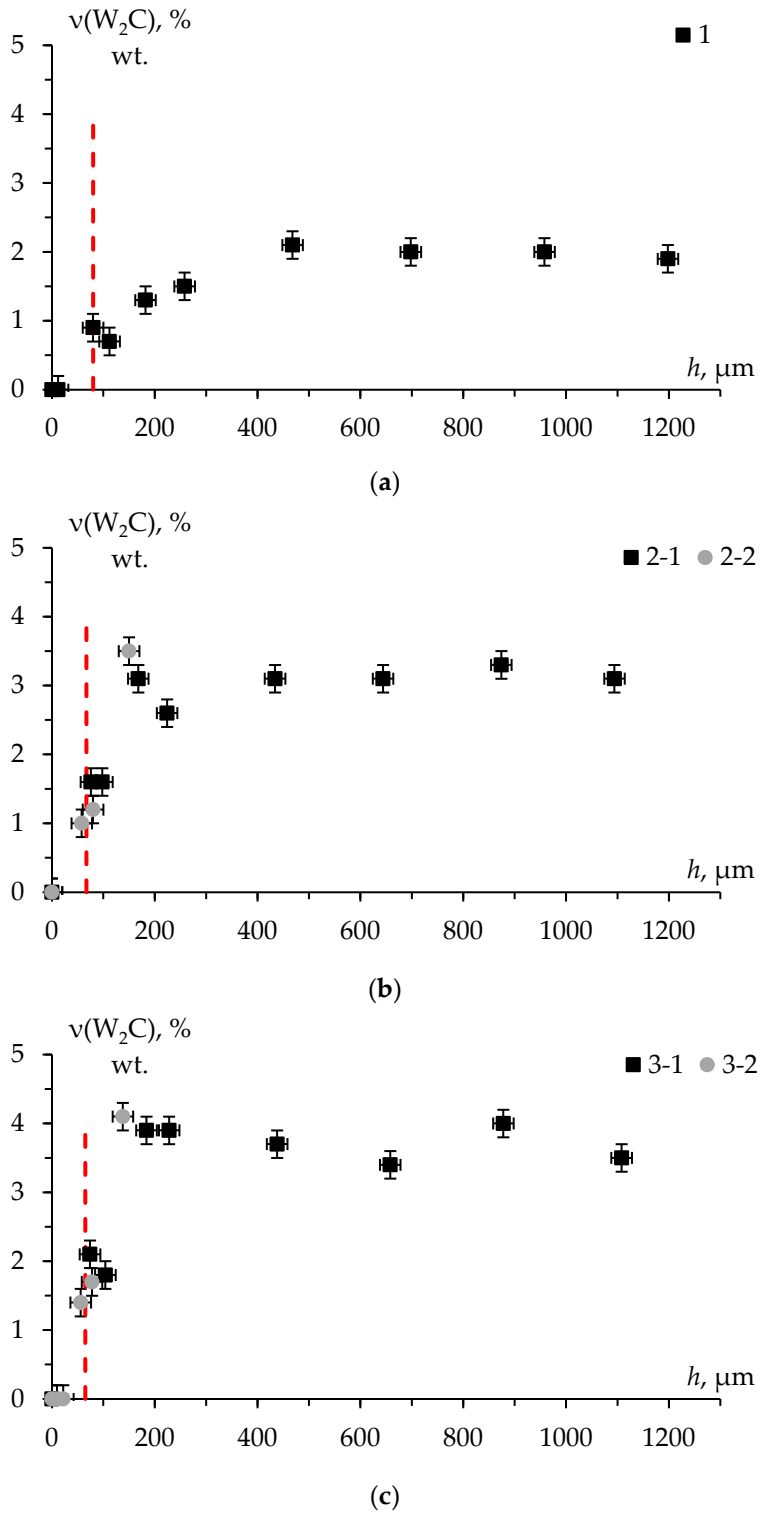

Figure 18. Dependence of W_2C mass fraction on the distance from the ceramic surface #1 (**a**), #2 (**b**), #3 (**c**). The red vertical line indicates the distance from the surface where the W_2C phase peaks were indicated on the XRD patterns.

According to the results of the XRD studies, there is the layer with a thickness of at least 50 μm that does not contain W_2C phase on the ceramic surface. According to the results of the SEM studies, abnormal grain growth processes are taking place in the surface layer. The phase composition of the specimens is a mixture of α-WC and W_2C phases in deeper layers. There is no significant difference in the mass fraction of W_2C phase at a depth of more than 200-300 μm.

Preprints (www.preprints.org) | NOT PEER-REVIEWED | Posted: 16 May 2023 doi:10.20944/preprints202305.1121.v1

As mentioned above, $W_2C \rightarrow \alpha$-WC phase change possible only in the presence of "free" carbon (equation (1)). It seems possible that the detection depth of W_2C phase corresponds to a rough estimation of the carbon diffusion depth into the ceramic surface. As can be seen from Figure 18, this value is at least 50 μm.

Due to the classical equation (solution of Fick's law) the diffusion layer thickness increases with the square root of the sintering time:

$$x_C = \sqrt{t \cdot D^*}, \quad (3)$$

t – the sintering time, D^* – the effective diffusion coefficient:

$$D^* = D_v + (\delta/d) \cdot D_b, \quad (4)$$

D_v – the volume diffusion coefficient of carbon in WC, D_b – the grain boundary diffusion coefficient of carbon in WC, δ – the grain boundary width ($\delta \approx 5 \cdot 10^{-10}$ m), d – the average grain size.

The diffusion coefficient temperature dependence may be written in the form:

$$D_i = D_{oi} \cdot \exp(-Q_i/kT), \quad (5)$$

D_{0i} – the pre-exponential diffusion factor, Q_i – the diffusion activation energy (in kT_m, T_m = 3143 K – the melting point of α-WC phase), k – the Boltzmann constant.

It has been demonstrated that the volume diffusion depth of carbon (^{14}C) of fine-grained tungsten carbide does not exceed 0.5 μm at temperature of 2370°C (the exposure time ~ 60 h) [36]. Table 1 presents the comparison of available literature data for the carbon diffusion activation energy and pre-exponential factor in tungsten carbide. The estimation of the carbon diffusion depth in WC according to the presented literature data was performed for powder **1**: T_1 = 1683 K, t_1 = 28.2 min, d_1 = 10^{-6} m.

Table 3. Carbon diffusion parameters in tungsten carbide.

Phase	Mechanism	D_0, m²/s	Q, kT_m	Reference	x_C, μm
α-WC	Volume	$1.9 \cdot 10^{-10}$	14.1	[36]	5
	Grain boundary	$4.6 \cdot 10^{-2}$	11.4		
	(*)	10^{-8}	9.3	[37]	1
W_2C	Volume	$1.8 \cdot 10^{-3}$	14.6	[38]	2
	Grain boundary	$1.8 \cdot 10^{-8}$	11.0		
	(*)	$6.7 \cdot 10^{-4}$	11.9	[39]	16
		$2 \cdot 10^{-4}$	13.6	[40]	2
		0.1	16.0	[41–43]	4
		30	20.0	[44, 45]	2

(*) There is no clarification about the carbon diffusion mechanism in a number of studies [37,39–45]. In this regard, it is assumed that the effective diffusion coefficient is specified.

The estimates of the carbon diffusion depth given in the paper (Figure 18) turn out to be significantly greater than the values calculated from the literature data (Table 3). It can thus be suggested that the effect of the abnormally deep carbon diffusion into tungsten carbide is observed in SPS process. The exact nature of this effect is not known.

It seems possible that there are three main factors contributing to a significant acceleration of the carbon diffusion process during SPS of tungsten carbide.

Firstly, it should be noted that SPS process of tungsten carbide is accompanied by plastic deformation of particles by the mechanism of power-law creep [46]. The strain can accelerate the carbon diffusion in the surface layers of ceramics based on tungsten carbide.

The second factor is the multistage process of W_2C particle formation at SPS, which can lead to an increase in the error in determining the carbon diffusion depth. Two processes (decarbonization and carburization) occur simultaneously during sintering of WC-based ceramics. The decarbonization process leads to an increase in the proportion of W_2C, and the carburization process causes a decrease in the proportion of W_2C. The rates of these processes may differ and have different

activation energy values. As a result of the addition of the two processes, non-monotonic character of the estimated carbon diffusion depth from the temperature and time of SPS process can be obtained.

The third factor to be taken into account is nonuniform distribution of thermal and electric fields at SPS [11,47,48]. In particular, overheating of the specimen surface at increased heating rates may cause an increase in the carbon diffusion depth. However, it is difficult to expect a large difference in the temperatures of the central and surface layers during sintering of tungsten carbide specimens. Therefore, it is assumed that the influence of this factor is insignificant.

5. Conclusions

The phase composition homogeneity of tungsten carbide specimens obtained by SPS was investigated. This study has shown that the phase composition and microstructure of the specimen surface layer significantly differs from the phase composition and microstructure of the central layer. The ceramic surface layers contain increased carbon concentration, which prevents the formation of W_2C particles and causes intensive grain growth. There is no significant dependence of the carburized layer depth on the initial particle size and sintering temperature. According to the results of the XRD studies, the carburized layer depth in the specimens was ~ 50 μm. The layer with a thickness of at least 50 μm with grains 10-50 times larger than the grain size in the main volume of the specimens is present near the surface. In the central layers of the ceramics, a uniform fine-grained microstructure and a homogeneous increased mass fraction of W_2C compared to the raw powders are observed.

It seems possible that changes in the phase composition and abnormal grain growth in the surface layers of tungsten carbide ceramics are due to abnormally deep carbon diffusion during sintering. The excess carbon source can be the material of a graphite mold and graphite punches, as well as graphite foil, which is used to reduce the clearance between the specimen and the inner surface of the mold. The current study found that the boron nitride coating does not completely eliminate the carburization effect of the surface layers of tungsten carbide ceramics.

Author Contributions: Methodology, V.C. and A.N.; investigation, K.S., E.L., A.M., M.B., N.I. and Y.B.; data curation, K.S. and P.A.; writing—original draft preparation, K.S.; writing—review and editing, K.S., P.A. and A.N.; supervision, V.C.; project administration, P.A. All authors have read and agreed to the published version of the manuscript.

Funding: This research was funded by Russian Science Foundation, grant number 22-73-10175.

Institutional Review Board Statement: Not applicable.

Informed Consent Statement: Not applicable.

Data Availability Statement: Data is contained within the article.

Conflicts of Interest: The authors declare no conflict of interest.

References

1. Gille, G.; Szesny, B.; et al. Submicron and ultrafine grained hardmetals for microdrills and metal cutting inserts. *Int. J. Refract. Met. Hard Mater.* **2022**, *20*, 3–22. doi: 10.1016/S0263-4368(01)00066-X
2. Zak Fang, Z.; Wang, X.; et al. Synthesis, sintering, and mechanical properties of nanocrystalline cemented tungsten carbide – A review. *Int. J. Refract. Met. Hard Mater.* **2009**, *27*, 288–299. doi: 10.1016/j.ijrmhm.2008.07.011
3. Shichalin, O.O.; Buravlev, I.Yu.; et al. SPS hard metal alloy WC-8Ni-8Fe fabrication based on mechanochemical synthetic tungsten carbide powder. *J. Alloys Compd.* **2020**, *816*, 152547. doi: 10.1016/j.jallcom.2019.152547
4. Shichalin, O.O.; Buravlev, I.Yu.; et al. Comparative study of WC-based hard alloys fabrication via spark plasma sintering using Co, Fe, Ni, Cr, and Ti binders. *Int. J. Refract. Met. Hard Mater.* **2022**, *102*, 105725. doi: 10.1016/j.ijrmhm.2021.105725
5. Sun, J.; Zhao, J.; et al. A Review on Binderless Tungsten Carbide: Development and Application. *Nanomicro Lett.* **2020**, *12*, 13. doi: 10.1007/s40820-019-0346-1

6. Gubernat, A.; Rutkowski, P.; et al. Hot pressing of tungsten carbide with and without sintering additives. *Int. J. Refract. Met. Hard Mater.* **2014**, *43*, 193–199. doi: 10.1016/j.ijrmhm.2013.12.002
7. Kim, H.-C.; Yoon, J.-K.; et al. Rapid sintering process and mechanical properties of binderless ultra fine tungsten carbide. *Mater. Sci. Eng. A* **2006**, *435–436*, 717–724. doi: 10.1016/j.msea.2006.07.127
8. Kim, H.-C.; Shon, I.J.; et al. Consolidation and properties of binderless sub-micron tungsten carbide by field-activated sintering. Int. *J. Refract. Met. Hard Mater.* **2004**, *22*, 257–264. doi: 10.1016/j.ijrmhm.2004.08.003
9. Tokita, M. Progress of Spark Plasma Sintering (SPS) Method, Systems, Ceramics Applications an Industrialization. *Ceramics* **2021**, *4*, 160-198. doi: 10.3390/ceramics4020014
10. Buravlev, I.Yu.; Shichalin, O.O.; et al. WC-5TiC-10Co hard metal alloy fabrication via mechanochemical and SPS techniques. *Int. J. Refract. Met. Hard Mater.* **2021**, *94*, 105385. doi: 10.1016/j.ijrmhm.2020.105385
11. Hu, Z.-Y.; Zhang, Z.-H.; et al. A review of multi-physical fields induced phenomena and effects in spark plasma sintering: Fundamentals and applications. *Mater. Des.* **2020**, *191*, 108662. doi: 10.1016/j.matdes.2020.108662
12. Olevsky, E.A.; Dudina, D.V. *Field-Assisted Sintering: Science and Applications*; Springer: Cham, Switzerland, 2018; p. 425. doi: 10.1007/978-3-319-76032-2
13. Cavaliere, P. *Spark Plasma Sintering of Materials*; Springer: Cham, Switzerland, 2019; p. 781. doi: 10.1007/978-3-030-05327-7
14. Isaeva, N.V.; Blagoveshchenskii, Yu.V.; et al. Preparation of nanopowders of carbides and hard-alloy mixtures applying low-temperature plasma. *Russ. J. Non-Ferr. Met.* **2014**, *55*, 585–591. doi: 10.3103/S1067821214060108
15. Lantsev, E.A.; Malekhonova, N.V.; et al. Spark plasma sintering of fine-grained WC hard alloys with ultra-low cobalt content. *J. Alloys Compd.* **2021**, *857*, 157535. doi: 10.1016/j.jallcom.2020.157535
16. Smetanina, K.E.; Andreev, P.V.; et al. Structural-phase features of WC-based ceramics obtained by the spark plasma sintering method. *IOP Conf. Ser. Mater. Sci. Eng.* **2021**, *1014*, 012053. doi: 10.1088/1757-899X/1014/1/012053
17. Lantcev, E.; Nokhrin, A.; et al. A Study of the Impact of Graphite on the Kinetics of SPS in Nano- and Submicron WC-10% Co Powder Compositions. *Ceramics* **2021**, *4*, 331–363. doi: 10.3390/ceramics4020025
18. Mouawad, B.; Soueidan, M.; et al. Full Densification of Molybdenum Powders Using Spark Plasma Sintering. *Metall. Mater. Trans. A* **2012**, *43*, 3402–3409. doi: 10.1007/s11661-012-1144-2
19. Bokhonov, B.B.; Ukhina, A.V.; et al. Carbon uptake during Spark Plasma Sintering: Investigation through the analysis of the carbide «footprint» in a Ni–W alloy. *RSC Adv.* **2015**, *5*, 80228–80237. doi: 10.1039/C5RA15439A
20. Morita, K.; Kim, B.N.; et al. Distribution of carbon contamination in oxide ceramics occurring during spark-plasma-sintering (SPS) processing: II – Effect of SPS and loading temperatures. *J. Eur. Ceram. Soc.* **2018**, *38*, 2596–2604. doi: 10.1016/j.jeurceramsoc.2017.12.004
21. Morita, K.; Kim, B.N.; et al. Fabrication of high-strength transparent $MgAl_2O_4$ spinel polycrystals by optimizing spark plasma sintering conditions. *J. Mater. Res.* **2009**, *24*, 2863–2872. doi: 10.1557/jmr.2009.0335
22. Wang, P.; Yang, M.; et al. Suppression of carbon contamination in SPSed CaF_2 transparent ceramics by Mo foil. *J. Eur. Ceram. Soc.* **2017**, *37*, 4103–4107. doi: 10.1016/j.jeurceramsoc.2017.04.070
23. Yong, S.M.; Choi, D.H.; et al. Study on carbon contamination and carboxylate group formation in Y_2O_3–MgO nanocomposites fabricated by spark plasma sintering. *J. Eur. Ceram. Soc.* **2020**, *40*, 847–851. doi: 10.1016/j.jeurceramsoc.2019.10.035
24. Li, H.; Khor, K.A.; et al. Microstructure modifications and phase transformation in plasma-sprayed WC–Co coatings following post-spray spark plasma sintering. *Surf. Coat. Technol.* **2005**, *194*, 96–102. doi: 10.1016/j.surfcoat.2004.04.075
25. Kurlov, A.S.; Gusev, A.I. *Tungsten Carbides. Structure, Properties and Application in Hardmetals*; Springer: Cham, Switzerland, 2013; p. 242. doi: 10.1007/978-3-319-00524-9
26. Krasovskii, P.V.; Blagoveshchenskii, Yu.V.; et al. Determination of oxygen in W-C-Co nanopowders. *Inorg. Mater.* **2008**, *44*, 954-959. doi: 10.1134/S0020168508090100
27. Kurlov, A.S.; Gusev, A.I. Vacuum annealing of nanocrystalline WC powders. *Inorg. Mater.* **2012**, *48*, 680–690. doi: 10.1134/S0020168512060088
28. Cha, S.I.; Hong, S.H. Microstructures of binderless tungsten carbides sintered by spark plasma sintering process. *Mater. Sci. Eng. A* **2003**, *356*, 381–389. doi: 10.1016/S0921-5093(03)00151-5

29. Poetschke, J.; Richter, V.; et al. Grain growth during sintering of tungsten carbide ceramics. *Int. J. Refract. Met. Hard Mater.* **2014**, *43*, 309–316. doi: 10.1016/j.ijrmhm.2014.01.001
30. Morton, C.W.; Wills, D.J.; et al. The temperature ranges for maximum effectiveness of grain growth inhibitors in WC–Co alloys. *Int. J. Refract. Met. Hard Mater.* **2005**, *23*, 287–293. doi: 10.1016/j.ijrmhm.2005.05.011
31. Li, T.; Li, Q.; et al. Abnormal grain growth of WC with small amount of cobalt. *Philos. Mag.* **2007**, *87*, 5657–5671. doi: 10.1080/14786430701694309
32. Yang, D.-Y.; Kang, S.-J.L. Suppression of abnormal grain growth in WC–Co via pre-sintering treatment. *Int. J. Refract. Met. Hard Mater.* **2009**, *27*, 90–94. doi: 10.1016/j.ijrmhm.2008.04.001
33. Yang, D.-Y.; Yoon, D.Y.; et al. Suppression of Abnormal Grain Growth in WC–Co via Two-Step Liquid Phase Sintering. *J. Am. Ceram. Soc.* **2011**, *94*, 1019–1024. doi: 10.1111/j.1551-2916.2010.04198.x
34. Reddy, K.M.; Rao, T.N.; et al. Stability of nanostructured W-C phases during carburization of WO_3. *Mater. Chem. Phys.* **2011**, *128*, 121–126. doi: 10.1016/j.matchemphys.2011.02.045
35. Yuan, J.; Zhan, Q.; et al. Decarburization mechanisms of WC–Co during thermal spraying: Insights from controlled carbon loss and microstructure characterization. *Mater. Chem. Phys.* **2013**, *142*, 165–171. doi: 10.1016/j.matchemphys.2013.06.052
36. Buhsmer, C.; Crayton, P. Carbon self-diffusion in tungsten carbide. *J. Mater. Sci.* **1971**, *6*, 981–988. doi: 10.1007/BF00549949
37. McCarty, L.V.; Donelson, R.; et al. A Diffusion Model for Tungsten Powder Carburization. *Metall. Mater. Trans. A* **1987**, *18*, 969–974. doi: 10.1007/BF02668545
38. Treheux, D.; Dubois, J.; et al. Bulk and grain boundary diffusion of ^{14}C in tungsten hemicarbide. *Ceram. Int.* **1981**, *7*, 142–148. doi: 10.1016/0272-8842(81)90011-0
39. Kharatyan, S.L.; Chatilyan, H.A.; et al. Kinetics of tungsten carbidization under non-isothermal conditions. *Mater. Res. Bull.* **2008**, *43*, 897–906. doi: 10.1016/j.materresbull.2007.05.003
40. Samsonov, G.V.; Vinitsky, I.M. *Refractory compounds*; Metallurgizdat: Moscow, Russia, 1976; p. 560. (In Russ.)
41. Lassner, E.; Schubert, W. *Tungsten: Properties, Chemistry, Technology of the Element, Alloys, and Chemical Compounds*; Springer: New York, US, 1999; p. 422. doi: 10.1007/978-1-4615-4907-9
42. Fries, R.J.; Cummings, J.E.; et al. Carbide layer-growth rates on tungsten-molybdenum and tungsten-rhenium alloys. *J. Nucl. Mater.* **1971**, *39*, 35–48. doi: 10.1016/0022-3115(71)90181-4
43. Andrews, M.R. Diffusion of Carbon through Tungsten and Tungsten Carbide. *J. Phys. Chem.* **1925**, *29*, 462–472. doi: 10.1021/j150250a010
44. Eremeev, V.S. Investigation of carbon diffusion from uranium monocarbide to molybdenum and tungsten. *At. Energy* **1968**, *25*, 489–493. (In Russ.)
45. Samsonov, G.V.; Epic, A.P. *Coatings made of refractory compounds*; Metallurgizdat: Moscow, Russia, 1964; p. 107. (In Russ.)
46. Lantsev, E.A.; Nokhrin, A.V.; et al. Study of high-temperature deformation features of ceramics of binderless tungsten carbide with various particle sizes. *Inorg. Mater. Appl. Res.* **2022**, *13*, 1324–1332. doi: 10.1134/S2075113322050240
47. Anselmi-Tamburini, U.; Gennari, S.; et al. Fundamental investigations on the spark plasma sintering/synthesis process II. Modeling of current and temperature distributions. *Mater. Sci. Eng. A* **2005**, *394*, 139–148. doi: 10.1016/j.msea.2004.11.019
48. Molenat, G.; Durand, L.; et al. Temperature control in spark plasma sintering: an FEM approach. *J. Metall.* **2010**, *2010*, 145431. doi: 10.1155/2010/145431